The Astrophysical Journal, 911:77 (8pp), 2021 April 20 https://doi.org/10.3847/1538-4357/abeaa8

The JAGWAR Prowls LIGO/Virgo O3 Paper I: Radio Search of a Possible Multimessenger Counterpart of the Binary Black Hole Merger Candidate S191216ap

D. Bhakta[1], K. P. Mooley[2,3], A. Corsi[1], A. Balasubramanian[1], D. Dobie[4,5,6], D. A. Frail[2], G. Hallinan[3], D. L. Kaplan[7], S. T. Myers[2], and L. P. Singer[8]
[1] Department of Physics and Astronomy, Texas Tech University, Box 41051, Lubbock, TX 79409-1051, USA; deven.r.bhakta@ttu.edu
[2] National Radio Astronomy Observatory, P.O. Box O, Socorro, NM 87801, USA
[3] Caltech, 1200 E. California Blvd. MC 249-17, Pasadena, CA 91125, USA
[4] Sydney Institute for Astronomy, School of Physics, University of Sydney, Sydney, New South Wales 2006, Australia
[5] ATNF, CSIRO Astronomy and Space Science, P.O. Box 76, Epping, New South Wales 1710, Australia
[6] ARC Centre of Excellence for Gravitational Wave Discovery (OzGrav), Hawthorn, Victoria, Australia
[7] Department of Physics, University of Wisconsin-Milwaukee, Milwaukee, WI, USA
[8] NASA/Goddard Space Flight Center, Greenbelt, MD 20771, USA
Received 2020 October 16; revised 2021 February 25; accepted 2021 February 26; published 2021 April 19

Abstract

We present a sensitive search with the Karl G. Jansky Very Large Array for the radio counterpart of the gravitational wave candidate S191216ap, which is classified as a binary black hole merger and suggested to be a possible multimessenger event, based on the detection of a high-energy neutrino and a TeV photon. We carried out a blind search at *C* band (4–8 GHz) over 0.3 deg^2 of the gamma-ray counterpart of S191216ap reported by the High-Altitude Water Cerenkov Observatory (HAWC). Our search, spanning three epochs over 130 days of postmerger and having a mean source-detection threshold of 75 μJy beam^{-1} (4σ), yielded five variable sources associated with active galactic nucleus activity and no definitive counterpart of S191216ap. We find $<$2% (3.0% $\pm$ 1.3%) of the persistent radio sources at 6 GHz to be variable on a timescale of $<$1 week (week–months), consistent with previous radio variability studies. Our 4σ radio luminosity upper limit of $\sim 1.2 \times 10^{28}$ erg s^{-1} Hz^{-1} on the afterglow of S191216ap, within the HAWC error region, is 5–10 times deeper than previous binary black hole (BBH) radio afterglow searches. Comparing this upper limit with theoretical expectations given by Perna et al. for putative jets launched by BBH mergers, for on-axis jets with energy $\simeq 10^{49}$ erg, we can rule out jet opening angles $\lesssim 20^\circ$ (assuming that the counterpart lies within the 1σ HAWC region that we observed).

Unified Astronomy Thesaurus concepts: Surveys (1671); Catalogs (205); Radio continuum emission (1340)

1. Introduction

Recent detections of high-energy neutrinos and gravitational waves (GWs) at extragalactic distances (Abbott et al. 2016; Aartsen et al. 2018) have ushered in a new age of "multimessenger" astronomy (Ando et al. 2013; Burns et al. 2019). The conventional electromagnetic (EM) branch of astronomy has played an important supporting role, helping to pinpoint the sources of the neutrinos and GW emission, and to constrain the physical properties of the progenitors (e.g., Abbott et al. 2017; Keivani et al. 2018). The study of these multimessenger events at radio wavelengths has been particularly rewarding. Important highlights include the detection of the first radio afterglow and direct imaging of relativistic outflow from the merger remnant GW170817 (Hallinan et al. 2017; Mooley et al. 2018a; Ghirlanda et al. 2019), and the imaging of the parsec-scale jet of the possible neutrino source TXS 0506+056 (Britzen et al. 2019; Li et al. 2020). In this paper we discuss the radio follow up of S191216ap, the first astrophysical source that may be both a source of GWs and neutrinos.

S191216ap was first reported as a compact binary merger candidate by the LIGO Scientific Collaboration (LSC) and Virgo Collaboration on 2019 December 16 at 21:33:38.473 UTC (LIGO Scientific Collaboration & Virgo Collaboration 2019a). The GW event was initially classified as a likely "mass-gap" signal, with one component of the binary having a mass between a definitive neutron star and black hole classification. The event was later reclassified with 99% probability as a binary black hole (BBH; LIGO Scientific Collaboration & Virgo Collaboration 2019b). The final (revised) sky map and distance was posted by the LSC and Virgo, with a 90% localization region of area 253 deg^2 and a luminosity distance estimate of 376 $\pm$ 70 Mpc (LIGO Scientific Collaboration & Virgo Collaboration 2019c).

The IceCube Neutrino Observatory reported a single muon neutrino in the direction of S191216ap, 43 s prior to the GW merger and with an overall *p*-value of 0.6% (2.5 σ) and an error radius of only $\pm 4^\circ$ (Hussain 2019; IceCube Collaboration 2019). Initially the High-Altitude Water Cerenkov Observatory (HAWC) reported no candidate gamma-ray events at TeV energies (HAWC Collaboration 2019a), but in a reanalysis of their data centered on the IceCube error region the HAWC collaboration reported a subthreshold event 80 s after the binary coalescence (HAWC Collaboration 2019b). This candidate gamma-ray event was found in a 10 s search and the significance level for this event is 4.6σ. This corresponds to a gamma-ray flux of about 7.3×10^{-9} TeV^{-1} cm^{-2} s^{-1} at 1 TeV for an intrinsic spectrum with an index of -2 (I. Martinez 2021, private communication). The coordinates[9] of the HAWC event are R.A.: 323.53 deg, decl: 5.23 deg, with the 68% containment region (radius) of 0.°3 (i.e., 0.28 deg^2 region; HAWC Collaboration 2019b).

[9] We note that these coordinates are outside the 90% credible region for S191216ap (but within the 98% credible region; LIGO Scientific Collaboration & Virgo Collaboration 2019c). The mean distance of S191216ap at the HAWC location is 286 $\pm$ 43 Mpc.

Table 1
Observing Log

No.	Start Date (UT)	Epoch	Δt (days)	Array Config.	rms (μJy bm^{-1})	BMAJ ($''$)	BMIN ($''$)	BPA (deg.)
1	2019 Dec 20 22:47:35	E1	4	D				
2	2019 Dec 21 21:49:45	E1	5	D	18	12.3	9.4	19
3	2019 Dec 22 00:00:36	E1	5	D				
4	2019 Dec 27 21:39:31	E2	11	D				
5	2019 Dec 27 23:50:21	E2	11	D	19	11.3	9.5	16
6	2019 Dec 28 21:22:14	E2	12	D				
7	2020 Apr 23 13:42:13	E3	129	C				
8	2020 Apr 23 15:53:03	E3	129	C	14	3.9	2.9	7.5
9	2020 Apr 24 13:38:17	E3	130	C				
10	2020 Aug 14 07:44:27	Follow-up	242	B	9–15	1.3	0.9	35

Note. The start date provides the time and date when each observation took place, with Δt reporting the number of days from the merger. We also report the rms (μJy bm^{-1}) for each epoch and the dimensions of the synthesized beam.

Many high-energy observatories were in operation during the S191216ap event, including the ANTARES neutrino detector (Ageron et al. 2019), Fermi GBM (Wood et al. 2019), MAXI GSC (Negoro et al. 2019), Swift/BAT (Palmer et al. 2019), CALET Gamma-Ray Burst Monitor (Sakamoto et al. 2019), AGILE (Verrecchia et al. 2019), AstroSAT (Shenoy & AstroSat CZTI Collaboration 2019), Insight-HXMT (Luo et al. 2019), and Konus-Wind (Ridnaia et al. 2020). A search for events both spatially and temporally coincident with S191216ap failed to find any likely counterpart high-energy candidates. A direct quantitative comparison between these nondetections and the HAWC detection is difficult, as most missions did not survey the entire error region and carried out photon searches in nonoverlapping time windows.

This possible multimessenger event set off a wave of deep searches at X-ray, optical/NIR and radio wavelengths within the first week. Search strategies were of two basic types (Nissanke et al. 2013), i.e., wide-area and galaxy-targeted searches. Nine galaxies were initially identified in the overlapping LIGO/Virgo-HAWC error region (Singer et al. 2019) and within the redshift range of S191216ap, a number that dropped to only three galaxies (Ahumada & Growth Collaboration 2019) after the revised LIGO/Virgo sky map was released (LIGO Scientific Collaboration & Virgo Collaboration 2019c). Targeted searches of these galaxies were made from radio to X-ray wavelengths (Mooley & Jagwar Team 2019; Sun et al. 2019; Xu et al. 2019; Yanagisawa et al. 2019; Zhu et al. 2019). Likewise, mosaicked observations were made of all or most of the LIGO/Virgo error region (Anand et al. 2019; Duverne 2019; Lundquist et al. 2019; McBrien et al. 2019; Zhu et al. 2019), or within the overlap region of LIGO/Virgo and IceCube or HAWC (Evans et al. 2019a, 2019b; Mooley et al. 2019; Ohgami et al. 2019; Rossi et al. 2019; Smith et al. 2019). With the exception of two optical transients from UKIRT, for which no follow up was undertaken (Smith et al. 2019), there were no compelling EM counterparts identified in that first week.

Accepting this preliminary identification of S191216ap as a multimessenger event, we conducted a search for radio counterparts as part of the Jansky Very Large Array (VLA) mapping of gravitational wave bursts as the Afterglows in Radio (JAGWAR) program. In Section 2 we describe the VLA observations, data processing imaging, and source catalog generation. In Section 3 we describe the search for variable/transient sources, finding no definitive radio counterpart for S191216ap. We end with a discussion of our results and future prospects for detecting the EM counterparts of BBH mergers.

2. Observations and Data Processing

2.1. VLA Observations

With consideration of the HAWC subthreshold event, we chose to conduct deep *C*-band (4–8 GHz) observations of the gamma-ray 68% containment region. To maximize the continuum imaging sensitivity, we used the Wide-band Interferometric Digital Architecture correlator with 32 spectral windows, 64 2 MHz wide channels each to get 4 GHz of total bandwidth centered on 6.0 GHz. Our observations were carried out across three epochs (E1, E2, E3), with each epoch being divided into three observations (for $\sqrt{3}$ improvement in sensitivity), with the Karl G. Jansky VLA in C and D array configurations, under the JAGWAR large program (VLA/18B-320; PI: Frail). The epoch time frame ranged from 5 days post merger to 4 months post merger (subject to scheduling constraints and sampling the putative afterglow light curve in logarithmic time steps). Each observation lasted for 3.6 hr and consisted of 37 pointings, with the goal of creating a standard pointed image mosaic of 0.38 deg^2 and achieve fairly uniform sensitivity across the 0.28 deg^2 HAWC region. The mosaic is centered on the coordinates reported for the HAWC subthreshold event (HAWC Collaboration 2019b). 3C 48 was used as the flux density and bandpass calibrator. The phase calibrator J2130+0502 was observed for a duration of 1 minute every 20–30 minutes. The observational parameters for all three epochs are listed in Table 1 for which we list for each epoch the array configuration, the rms noise (rms), and the synthesized beam (BMAJ, BMIN, BPA) of each final image. Figure 1 shows the image mosaic along with the locations of the VLA pointings and the HAWC 68% confidence region.

We conducted follow-up observations in the *C* band of any significant variable sources identified with the mosaicked region. These pointed observations were carried out on 2020 August 14 with the VLA in the *B*-array configuration (see Table 1). Integration times varied from ≈4–10 minutes, depending on the flux density of the sources. The total duration of the observation was 47 minutes. 3C 48 was used as the flux density and bandpass calibrator, while the phase calibrator was J2130+0502.

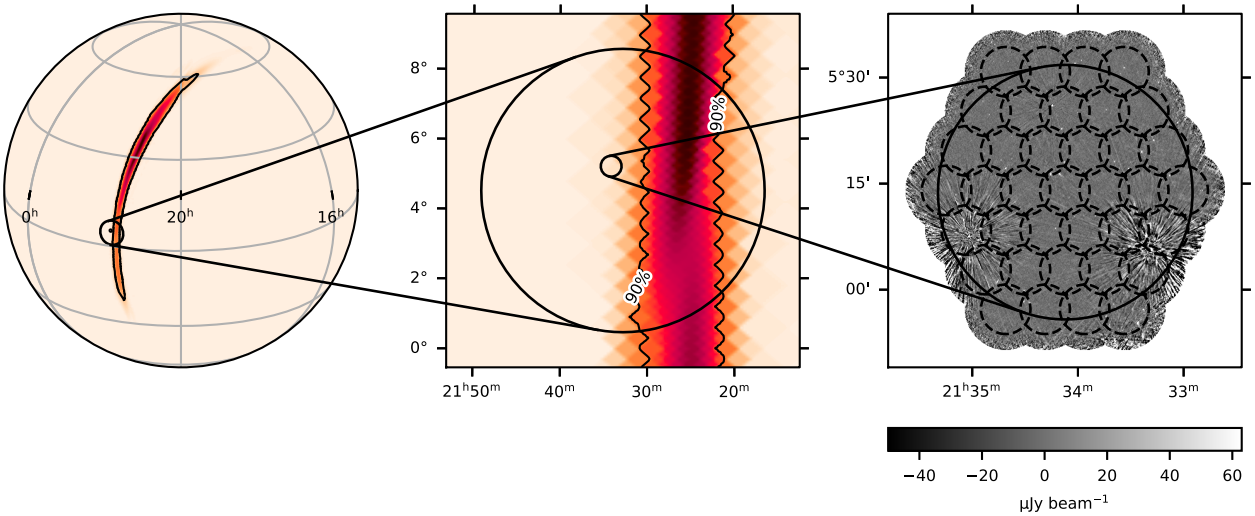

Figure 1. The LIGO/Virgo sky localization of S191216ap (left) shown along with the localization regions for the IceCube (larger circle, 90% containment) and HAWC events (smaller circle 0.28 deg^2, 68% containment: middle panel). The right panel shows the sky coverage of our VLA follow up observations of the HAWC 68% containment region. The 0.38 deg^2 image mosaic is from our epoch E3 (see Table 1). The larger black circle corresponds to the 0.28 deg^2 HAWC region, while the smaller circles correspond to the primary beams (half-power beamwidth of about 7′) of the 37 pointings at *C* band (central frequency of 6 GHz). The gray-scale bar displays the pixel values, going from -50 μJy beam^{-1} (black) to 63 μJy beam^{-1} (white).

2.2. RFI Flagging, Calibration, and Imaging

Directly after the observations for each epoch were completed, we downloaded the raw data from the VLA archive onto the Lustre file system at the NRAO AOC in Socorro. The raw data was then calibrated using the NRAO CASA pipeline (in CASA 5.6.1). Post calibration, we carried out manual flagging to remove the spectral windows affected by residual RFI. For the imaging, we used CASA `clean` with Briggs weighting (robust factor of 0.5), two Taylor terms, and a threshold of 0.1 mJy. The pixel size was chosen to sample the synthesized beam across six pixels for the first two epochs and four pixels for the third epoch. The central frequency for each image is 6.0 GHz.

Linear mosaicking of the 37 single-pointing images for each epoch was then carried out using `FLATN` in AIPS. The mosaics for the first two epochs are 1500×1500 pix^2 and the third epoch is 3000×3000 pix^2. The primary beam parameters were acquired from EVLA Memo 195[10] during the linear mosaicking step. Figure 2 shows the cumulative rms noise plots for the three image mosaics.

We followed an identical procedure for the variable source observations. After running the VLA automated calibration pipeline, we split that data set into individual measurement sets. Then we checked the phase calibrator and the flux calibrators for any RFI from antennae or spectral windows, before proceeding with flagging and clipping. For our imaging, we used almost identical parameters, with the change being image size and cell size to accommodate the array configuration change.

2.3. Source Cataloging, Point Source Selection, and Flux Density Correction

We used the Search and Destroy (SAD) task within AIPS to generate 4σ catalogs for each of our three image mosaics.

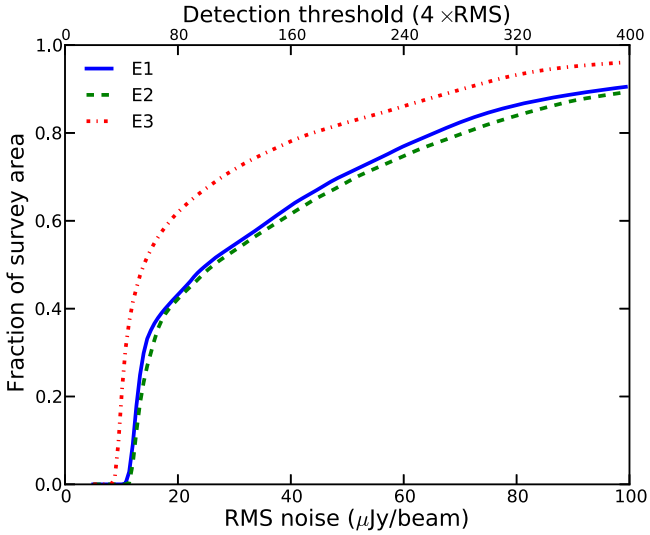

Figure 2. Cumulative rms noise across the 0.38 deg^2 survey region for the three epochs of observations (E1, E2, and E3). The source-detection threshold (4σ) is shown on the upper *x*-axis. The 50% completeness over the 0.28 deg^2 HAWC region corresponds to an rms noise of about 16 μJy for epochs E1 and E2, and about 10 μJy for epoch E3.

These catalogs contain around 360 sources for epochs E1 and E2 and around 780 sources[11] for epoch E3. For a source beyond 200 Mpc, we do not expect contaminating radio emission from any putative host galaxy (Hotokezaka et al. 2016; Mooley et al. 2018b) of the candidate merger, and hence we shortlisted only the point sources for the transient and variability search. Our criteria for selecting point-like sources and rejecting false positives (resulting from image artifacts

[10] Perley (2016), https://library.nrao.edu/public/memos/evla/EVLAM_195.pdf.

[11] The increase in the number of sources detected is due to the reduced image noise in E3 and sources (AGN) from E1/E2 being resolved into doubles in E3 (due to the factor of 2 increase in angular resolution between D and C array configurations).

around bright sources) were the same as those used in some previous works (Mooley et al. 2016; Hajela et al. 2019):

1. BMAJ/1.7 < MAJ < 1.7 × BMAJ
2. BMIN/1.7 < MIN < 1.7 × BMIN,
3. BMAJ/BMIN < 2.5
4. 0.67 < Flux/Peak < 1.5

where BMAJ and BMIN are the major and minor axes of the synthesized beam, MAJ, MIN, Flux, and Peak are the major and minor axes of the fitted Gaussian and the integrated and peak-flux densities as reported by SAD. The first three criteria are motivated by thorough inspection of archival VLA images and source catalogs, and help in differentiating side lobes (false positives) and spike-like imaging artifacts seen occasionally around bright sources in VLA images. They also allow extended source rejection. The fourth is a simplified criterion for differentiating between resolved and point-like sources (see Figure 9 of Smolčić et al. 2017). We then generated a single point-source catalog (PSC) by merging the list of point-like sources for all three epochs. The PSC had tens of sources that were present in epoch E3 at the 4–5 σ level and absent in epochs E2 and E3. We rejected these sources as false positives after inspecting both the catalog and image mosaic as being due to noise/imaging artifacts, and compiled the final PSC containing 165 sources. For all sources in the PSC we plotted a histogram of the ratio of peak-flux densities between E1–E2 and E1–E3, and found that flux multiplicative factors of 0.94 and 1.1 were necessary for epochs E2 and E3, respectively, in order to make the histograms centered on unity. We therefore corrected all peak flux densities in E2 and E3 accordingly in the PSC.

3. Transient and Variability Search

We used the PSC from Section 2.2 to carry out a search for transients sources that appeared or disappeared in one or more of the three epochs. No transients were found to a 4σ limit of ~75 μJy (mean completeness threshold for the merged catalog over three epochs and 100 deg^2).

Following Mooley et al. (2016) we used the PSC to also investigate two-epoch variability using the variability statistic, $V_s = \Delta S/\sigma$ and modulation index $m = \Delta S/\bar{S}$, where S is the flux density, $\bar{S}$ is the average flux density over the two epochs being compared, ΔS is the flux density difference, and σ is the rms noise. We used epoch E1 as the reference and performed the following two-epoch comparisons: E1–E2 and E1–E3. Significant variables were identified as those sources having $|V_s|$ larger than three (corresponding to a Gaussian equivalent of approximately 3σ, i.e., a chance probability of finding three variables out of 1000 sources, which ensures that less than one false positive will be detected as a variable source in our search, assuming Gaussian statistics) and the absolute value of the modulation index, $|m|$, larger than 0.18 (i.e., a fractional variability, $f_{\rm var} > 1.2$, which was chosen while bearing in mind that flux correction factors of up to 10% were applied to the flux densities within the PSC and that our flux scale is accurate to only ~5%).

The plot of the variability statistic versus the modulation index is shown in Figure 3. We found no significant variable sources in the E1–E2 comparison (probing a timescale of <1 week) and five significant variables in the E1–E3 comparison (probing a timescale of <4 months). This indicates that <2% of the persistent sources are variable on <1 week timescale and

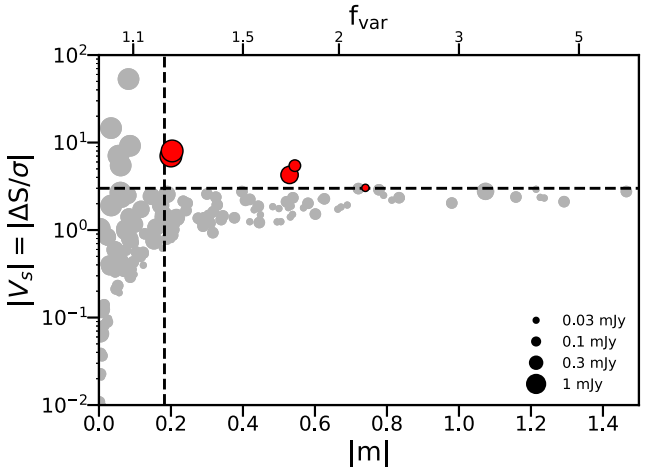

Figure 3. Variability statistic (V_s) vs. the modulation index (m) for the 165 sources in our PSC. Gray points indicate sources (from the E1–E2 and E1–E3 comparisons) that are not significant variables. The red points are the selected variables between E1–E3 (five sources, see Table 2). No significant variables were found in the E1–E2 comparison. The black dashed lines indicates the variability selection criteria in $|V_s|$ and $|m|$ (see Section 3). The flux densities of the sources define the marker size (shown in the legend). The top horizontal scale is the fractional variability $f_{\rm var}$, defined as the ratio of the flux densities between two epochs being compared. See Section 3 for details.

3.0% ± 1.3% of the persistent sources are variable on timescales of week–months. This level of variability is typical for the radio sky (e.g., Carilli et al. 2003; Bell et al. 2015; Hancock et al. 2016; Mooley et al. 2016) and at these frequencies it is attributed to normal activity from active galactic nuclei (AGNs; Radcliffe et al. 2019).

Next we examine the properties of these five variable sources for any indication that they may be long-lived transients related to S191216ap and not just background AGN. Their properties are summarized in Table 2. Radio data include the source positions (R.A./decl.), the flux densities for all three epochs (S1, S2, S3), the modulation index (m), the variability statistic (V_s), and the in-band spectral indices (α) for the first (E1) and third epochs (E3). Also included are the results of WISE counterpart source matching (Wright et al. 2010) in which we attempted to classify the radio source using WISE colors from the AllWise Catalog (Cutri et al. 2013) and Nikutta et al. (2014). Finally, we used the latest release of the Sloan Digital Sky Survey (SDSS DR14) in which we record the r-band magnitude and the photometric redshifts where available for each WISE source.

We found WISE counterparts for four JAGWAR sources: J213250+051359, J213317+052104, J213341+051946, and J213453+052633. The remaining JAGWAR source, J213407+051800, is located 11.″6 from AllWISE J213407.27+051804.8, with rmag = 20.8 and a photometric redshift of 0.44. None of these five sources are in the WISE AGN catalog of Assef et al. (2018). From their WISE colors we deduce from Wright et al. (2010) that the putative hosts are variously luminous infrared galaxies (LIRGs), spirals, and/or elliptical galaxies (see Table 2). Two sources, J213317+052104 and J213453+052633, have photometric redshift values that place the host galaxy far beyond the luminosity distance of S191216ap.

The light curves are shown in Figure 4. They include the VLA follow-up observations from day 242 (see Table 1). We detected all of five sources at integrated flux densities of

Table 2
Summary of Variables Sources

Name (JAGWAR J...)	R.A. (deg)	Decl. (deg)	S1 (μJy)	S2 (μJy)	S3 (μJy)	S_F (μJy)	m	Vs	$\alpha_{4.9}^{7.0}$(E3)	Host Ident.	r (mag)	Phot-z
E1–E2 comparison; Timescale <1 week												
None												
E1–E3 comparison; Timescale <4 months												
J213250+051359	323.20873	5.23317	263 ± 21	255 ± 23	139 ± 15	134 ± 15	0.53	4.3	-1.0 ± 0.4	LIRG	17.5	0.09 ± 0.02
J213317+052104	323.32286	5.35130	742 ± 15	881 ± 16	552 ± 12	558 ± 14	0.20	7.0	-0.5 ± 0.1	Spiral/Ellip.	22.4	0.97 ± 0.11
J213341+051946	323.42447	5.32948	44 ± 13	49 ± 12	87 ± 11	58 ± 9	−0.74	−3.0	-1.2 ± 0.8	LIRG/Spiral	>22.7	…
J213407+051800	323.53327	5.30004	808 ± 15	956 ± 15	599 ± 11	830 ± 15	0.20	8.0	-0.4 ± 0.1	…	>22.7	…
J213453+052633	323.72386	5.44276	124 ± 13	123 ± 13	197 ± 11	244 ± 15	−0.54	−5.4	$+0.3 \pm 0.3$	LIRG	22.1	0.61 ± 0.09

Note. By investigating the use of two-epoch variability (with Epoch 1 as our reference epoch), we found no variable sources over E1–E2 and five variable sources over E1–E3. The flux of each JAGWAR source is reported in columns S1, S2, S3, and S_F, corresponding to each epoch and the follow-up observation. The modulation index ($m = \Delta S/\bar{S}$) and the Variability Index ($V_s = \Delta S/\sigma$) for each source are calculated and provided in columns m and V_s. The host identities were determined using the WISE colors (Wright et al. 2010) calculated from the ALLWise Catalog (Cutri et al. 2013) after checking whether the source matched any AGN sources. The r-band magnitude and the spectroscopic redshift were acquired from SDSS DR14. J213341+051946 was initially not detected in Epoch 1 so no in-band spectral index was calculated for Epoch 1.

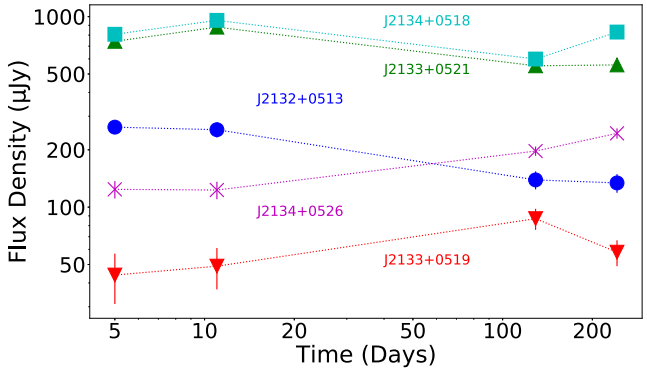

Figure 4. Radio light curves at 6 GHz for the five variable sources identified in Table 2. The *x*-axis gives the time since the merger. Flux densities for each source are shown in different shapes (circle, triangle, inverted triangle, square, and star).

134 ± 15 μJy, 558 ± 14 μJy, 58 ± 9 μJy, 830 ± 15 μJy, 244 ± 10 μJy, respectively (in the order listed in Table 2). With only four epochs, it is not easy to make any definitive statements, but they are consistent with fluctuations from persistent radio sources and none of the sources show the sharp rise and decay pattern of an afterglow. J213453+052633 exhibits a rise, nearly doubling during the 242 days. However, the photometric redshift of its host galaxy rules out an association with S121916ap. The brightest radio source J213407+051800 is also detected in the first-look images of the VLA Sky Survey (VLASS) with a 3 GHz flux density of 569 ± 122 μJy, from data taken on 2017 October 20 (Lacy et al. 2020). None of the other radio sources were detected in the VLASS with 3 σ limits $\leqslant$375 μJy. Finally we note that in the higher resolution follow-up observations, JAGWAR J213250+051359 clearly shows a core-jet morphology.

Based on the host galaxy classifications and redshifts, plus the amplitude, timescale, and fractional variation level, persistence of the radio emission and radio source morphology, it seems likely that these variable radio sources are background low-luminosity AGN and likely unrelated to S191216ap.

4. Discussion and Future Prospects

Stellar mass binary black hole mergers were not widely expected to generate EM counterparts, so early predictions focused on EM signatures from binary NSs and BH–NS binaries (e.g., Metzger & Berger 2012; Nissanke et al. 2013). Nevertheless, observations were still undertaken to search for incoherent radio emission in the first two science runs of LIGO (Palliyaguru et al. 2016; Mooley et al. 2018b; Artkop et al. 2019). Another promising avenue has been the search for prompt *coherent* radio emission on timescales of minutes to hours post merger, using wide-field low-frequency arrays (Yancey et al. 2015; Kaplan et al. 2016; Callister et al. 2019; James et al. 2019; Rowlinson & Anderson 2019). Renewed impetus for afterglow searches came following the nominal detection (2.9σ) of a gamma-ray flare from Fermi-GBM detection toward GW150914 (Connaughton et al. 2016, 2018). This stimulated a number of theoretical investigations for stellar mass BBHs (e.g., Loeb 2016; Perna et al. 2016; Woosley 2016; Zhang 2016), which in several cases predict specific EM signatures that are testable with follow-up radio observations (Morsony et al. 2016; Yamazaki et al. 2016; Perna et al. 2019).

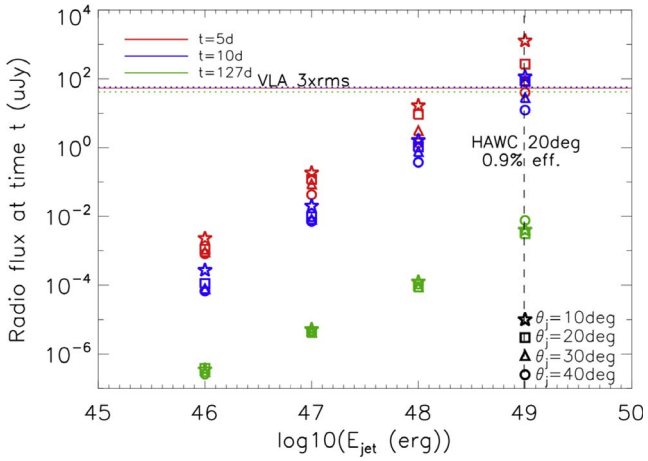

Figure 5. Sensitivity reached in our VLA follow up (horizontal lines; see also see Table 1) with models for potential BBH radio afterglows as seen from an on-axis observer (symbols; Perna et al. 2019). See Section 4 for details.

As noted earlier (Section 1), S191216ap has been classified as a BBH merger event seen by LIGO/Virgo, which had a coincident neutrino detection from IceCube, and a possible detection of an EM counterpart at TeV energies from HAWC. We have carried out a search for a radio transient within the HAWC error circle for three epochs covering timescales between 4 days and 4 months at a wavelength of 6 cm (Section 2.2). While no radio transients were discovered, our flux density upper limits represent a considerable improvement over past BBH radio afterglow searches. Our 4σ limits[12] of 75 μJy for a radio afterglow from S191216ap is an improvement over the 4σ radio limits of 600 μJy limits for GW151226 (Mooley et al. 2018b) and 180 μJy for GW170608 (Artkop et al. 2019), two BBH events that occurred during the O2 and O3 Virgo science runs, respectively. Factoring in the luminosity distance of S191216ap, the radio luminosity is 1.2×10^{28} erg s^{-1} Hz^{-1}, or approximately 5–10 times deeper than these previous BBH radio afterglow searches.

Given the absence of a radio transient for this GW/neutrino/TeV candidate event, we next look at how our radio limits can be used to set limits on any putative afterglow from S191216ap. We adopt the model of Perna et al. (2019), in which a jet is formed during the BBH merger that propagates freely, without any baryonic contamination from tidal disrupted material, until it interacts with the surrounding interstellar medium and generates afterglow emission. In Figure 5 we compare the sensitivity reached in our VLA follow up (horizontal lines; see also see Table 1) with models for potential BBH radio afterglows as seen from an on-axis observer. The model predictions at timescales comparable to those of our radio follow up are shown for different values of the total kinetic energy in the jet ($E_{\rm jet}$) and of the jet half-opening angle θ_j (symbols; Perna et al. 2019). We have rescaled the model values provided at 1.4 GHz by Perna et al. (2019) to 6 GHz assuming an optically thin spectral index of 0.65, which is consistent with the model itself between radio and optical frequencies. These model predictions also assume $\Gamma = 100$, $\epsilon_e = 0.03$, $\epsilon_B = 0.01$, and $n_{\rm ISM} = 0.01$ cm^{-3} (Perna et al. 2019). We note that the observed fluxes scale as $n^{5/14}$ for a fully radiative blast wave and as $n^{1/2}$ for an adiabatic evolution. Thus, generally speaking, higher densities imply

[12] This is the mean sensitivity across the HAWC region.

larger fluxes (Perna et al. 2019). Given the tentative HAWC subthreshold event at 1 TeV, we focus our comparison on the $\Gamma = 100$ (highly relativistic jet) models presented in Perna et al. (2019) rather than on the $\Gamma = 10$ (mildly relativistic jet) case.

As is evident from Figure 5, our radio follow-up campaign was sensitive to only the most optimistic EM counterpart models in terms of energy coupled to a relativistic ejecta. For reference, in Figure 5 we also mark with a vertical dashed line an order-of-magnitude energy estimate derived from the flux density measurement of the HAWC subthreshold event at 1 TeV as (HAWC Collaboration 2019b):

$$E_{\rm HAWC} \sim (1\ {\rm TeV})^2 \times 7.3 \times 10^{-9}\ {\rm TeV^{-1}\,cm^{-2}\,s^{-1}} \times 10\ {\rm s} \times \frac{4\pi d_L^2 (1 - \cos(20\ {\rm deg}))}{\xi}, \quad (1)$$

where we neglect redshift corrections, we set $d_L = 320$ Mpc, have assumed a high-energy signal duration of 10 s, a jet opening angle of 20 deg, and an efficiency of $\xi = 0.9\%$ for the conversion of ejecta kinetic energy into prompt emission energy at 1 TeV. This value of the efficiency is chosen so that the flux density measured by HAWC is consistent with the hypothesis of a BBH jet with kinetic energy of 10^{49} erg (and opening angle of 20 deg), which is the minimum energy value for which our radio upper limits are constraining of the model predictions.

Our work has a number of limitations. In particular, our VLA imaging campaign focused on the area defined by the HAWC error circle (HAWC Collaboration 2019b). If the gamma-ray emission (or neutrino detection) were were not deemed significant, then the multimessenger aspect of this event would be in question, and we would have surveyed less than 0.1% of the full error region of S191216ap. Furthermore, even though the observations presented here are an improvement in sensitivity over earlier LIGO/Virgo science runs, the current radio limits are still not sufficiently constraining on all predicted EM signatures from BBHs. For example, radio methods are also not particular powerful for finding EM signatures from BBH mergers in accretion disk environments of supermassive BHs (Bartos et al. 2017; Stone et al. 2017; McKernan et al. 2019; Tagawa et al. 2020), a model invoked to argue that a peculiar optical flaring AGN was the counterpart of the GW event S190521g (Graham et al. 2020). Radio is well suited for identifying transients, but radio variability is most commonly ascribed to regular AGN variability. Nonetheless, the phase space remains large for both prompt and longer-term searches for coherent and incoherent radio emission, respectively. Such searches should continue during the fourth GW science run which should include the Kamioka Gravitational Wave Detector detector, with array improvements in both sensitivity and localization (Abbott et al. 2018). The detection of radio afterglow from a BBH would revolutionize the studies of such objects in much the same way that the multimessenger studies of GW170817 advanced our understanding of binary neutron stars.

The National Radio Astronomy Observatory is a facility of the National Science Foundation operated under cooperative agreement by Associated Universities, Inc. We would like to thank the NRAO staff, especially Amy Mioduszewski, Heidi Medlin, Drew Medlin, Tony Perreault and Abi Smoake for help with observation scheduling and computing. K.P.M. is currently a Jansky Fellow of the National Radio Astronomy Observatory. K.P.M. and G.H. acknowledge support from the National Science Foundation Grant AST-1911199. A.C., A.B., and D.B. acknowledge support from the National Science Foundation via the CAREER grant #1455090. D.K. is supported by NSF grant AST-1816492.

ORCID iDs

D. Bhakta https://orcid.org/0000-0002-7965-3076
K. P. Mooley https://orcid.org/0000-0002-2557-5180
A. Corsi https://orcid.org/0000-0001-8104-3536
A. Balasubramanian https://orcid.org/0000-0003-0477-7645
D. Dobie https://orcid.org/0000-0003-0699-7019
G. Hallinan https://orcid.org/0000-0002-7083-4049
D. L. Kaplan https://orcid.org/0000-0001-6295-2881
L. P. Singer https://orcid.org/0000-0001-9898-5597

References

Aartsen, M. G., Ackermann, M., Adams, J., et al. 2018, Sci, 361, 147
Abbott, B. P., Abbott, R., Abbott, T. D., et al. 2016, PhRvL, 116, 061102
Abbott, B. P., Abbott, R., Abbott, T. D., et al. 2017, ApJL, 848, L12
Abbott, B. P., Abbott, R., Abbott, T. D., et al. 2018, LRR, 21, 3
Ageron, M., Baret, B., Coleiro, A., et al. 2019, GCN Circ., 26458, 1, https://gcn.gsfc.nasa.gov/gcn3/26458.gcn3
Ahumada, T. & Growth Collaboration 2019, GCN Circ., 26507, 1, https://gcn.gsfc.nasa.gov/gcn/gcn3/26507.gcn3
Anand, S., Ahumada, T., Bellm, E., et al. 2019, GCN Circ., 26464, 1, https://gcn.gsfc.nasa.gov/gcn/gcn3/26464.gcn3
Ando, S., Baret, B., Bartos, I., et al. 2013, RvMP, 85, 1401
Artkop, K., Smith, R., Corsi, A., et al. 2019, ApJ, 884, 16
Assef, R. J., Stern, D., Noirot, G., et al. 2018, ApJS, 234, 23
Bartos, I., Kocsis, B., Haiman, Z., & Márka, S. 2017, ApJ, 835, 16
Bell, M. E., Huynh, M. T., Hancock, P., et al. 2015, MNRAS, 450, 4221
Britzen, S., Fendt, C., Böttcher, M., et al. 2019, A&A, 630, A103
Burns, E., Tohuvavohu, A., Bellovary, J. M., et al. 2019, BAAS, 51, 250
Callister, T. A., Anderson, M. M., Hallinan, G., et al. 2019, ApJL, 877, L39
Carilli, C. L., Ivison, R. J., & Frail, D. A. 2003, ApJ, 590, 192
Connaughton, V., Burns, E., Goldstein, A., et al. 2016, ApJL, 826, L6
Connaughton, V., Burns, E., Goldstein, A., et al. 2018, ApJL, 853, L9
Cutri, R. M., et al. 2013, VizieR On-line Data Catalog, II/328
Duverne, P. A. 2019, GCN Circ., 26528, 1, https://gcn.gsfc.nasa.gov/gcn/gcn3/26528.gcn3
Evans, P. A., Keivani, A., Kennea, J. A., et al. 2019a, GCN Circ., 26475, 1, https://gcn.gsfc.nasa.gov/gcn/gcn3/26475.gcn3
Evans, P. A., Kennea, J. A., Tohuvavohu, A., et al. 2019b, GCN Circ., 26498, 1, https://gcn.gsfc.nasa.gov/gcn/gcn3/26498.gcn3
Ghirlanda, G., Salafia, O. S., Paragi, Z., et al. 2019, Sci, 363, 968
Graham, M. J., Ford, K. E. S., McKernan, B., et al. 2020, PhRvL, 124, 251102
Hajela, A., Mooley, K. P., Intema, H. T., et al. 2019, MNRAS, 490, 4898
Hallinan, G., Corsi, A., Mooley, K. P., et al. 2017, Sci, 358, 1579
Hancock, P. J., Drury, J. A., Bell, M. E., et al. 2016, MNRAS, 461, 3314
HAWC Collaboration 2019a, GCN Circ., 26455, 1, https://gcn.gsfc.nasa.gov/gcn/gcn3/26455.gcn3
HAWC Collaboration 2019b, GCN Circ., 26472, 1, https://gcn.gsfc.nasa.gov/gcn/gcn3/26472.gcn3
Hotokezaka, K., Nissanke, S., Hallinan, G., et al. 2016, ApJ, 831, 190
Hussain, R. 2019, GCN Circ., 26463, 1, https://gcn.gsfc.nasa.gov/gcn/gcn3/26463.gcn3
IceCube Collaboration 2019, GCN Circ., 26460, 1, https://gcn.gsfc.nasa.gov/gcn/gcn3/26460.gcn3
James, C. W., Anderson, G. E., Wen, L., et al. 2019, MNRAS, 489, L75
Kaplan, D. L., Murphy, T., Rowlinson, A., et al. 2016, PASA, 33, e050
Keivani, A., Murase, K., Petropoulou, M., et al. 2018, ApJ, 864, 84
Lacy, M., Baum, S. A., Chandler, C. J., et al. 2020, PASP, 132, 035001
Li, X., An, T., Mohan, P., et al. 2020, ApJ, 896, 63
LIGO Scientific Collaboration, & Virgo Collaboration 2019a, GCN Circ., 26454, 1, https://gcn.gsfc.nasa.gov/gcn/gcn3/26454.gcn3
LIGO Scientific Collaboration, & Virgo Collaboration 2019b, GCN Circ., 26570, 1, https://gcn.gsfc.nasa.gov/gcn/gcn3/26570.gcn3

LIGO Scientific Collaboration, & Virgo Collaboration 2019c, GCN Circ., 26505, 1, https://gcn.gsfc.nasa.gov/gcn/gcn3/26505.gcn3
Loeb, A. 2016, ApJL, 819, L21
Lundquist, M. J., Sand, D. J., Fong, W.-F., et al. 2019, GCN Circ., 26473, 1, https://gcn.gsfc.nasa.gov/gcn/gcn3/26473.gcn3
Luo, Q., Zheng, Y. G., Cai, C., et al. 2019, GCN Circ., 26569, 1, https://gcn.gsfc.nasa.gov/gcn/gcn3/26569.gcn3
McBrien, O., Smartt, S. J., Smith, K. W., et al. 2019, GCN Circ., 26563, 1, https://gcn.gsfc.nasa.gov/gcn/gcn3/26563.gcn3
McKernan, B., Ford, K. E. S., Bartos, I., et al. 2019, ApJL, 884, L50
Metzger, B. D., & Berger, E. 2012, ApJ, 746, 48
Mooley, K. & Jagwar Team 2019, GCN Circ., 26530, 1, https://gcn.gsfc.nasa.gov/gcn/gcn3/26530.gcn3
Mooley, K., Myers, S., Frail, D., et al. 2019, GCN Circ., 26531, 1, https://gcn.gsfc.nasa.gov/gcn/gcn3/26531.gcn3
Mooley, K. P., Deller, A. T., Gottlieb, O., et al. 2018a, Natur, 561, 355
Mooley, K. P., Frail, D. A., Myers, S. T., et al. 2018b, ApJ, 857, 143
Mooley, K. P., Hallinan, G., Bourke, S., et al. 2016, ApJ, 818, 105
Morsony, B. J., Workman, J. C., & Ryan, D. M. 2016, ApJL, 825, L24
Negoro, H., Kawai, N., Sugita, S., et al. 2019, GCN Circ., 26462, 1, https://gcn.gsfc.nasa.gov/gcn/gcn3/26462.gcn3
Nikutta, R., Hunt-Walker, N., Nenkova, M., et al. 2014, MNRAS, 442, 3361
Nissanke, S., Kasliwal, M., & Georgieva, A. 2013, ApJ, 767, 124
Ohgami, T., Tominaga, N. & J-GEM collaboration 2019, GCN Circ., 26509, 1, https://gcn.gsfc.nasa.gov/gcn/gcn3/26509.gcn3
Palliyaguru, N. T., Corsi, A., Kasliwal, M. M., et al. 2016, ApJL, 829, L28
Palmer, D. M., Barthelmy, S. D., Lien, A. Y., et al. 2019, GCN Circ., 26466, 1, https://gcn.gsfc.nasa.gov/gcn/gcn3/26466.gcn3
Perley, R. 2016, Jansky Very Large Array Primary Beam Characteristics, Tech. Rep., EVLA Memo 195, https://library.nrao.edu/public/memos/evla/EVLAM_195.pdf
Perna, R., Lazzati, D., & Farr, W. 2019, ApJ, 875, 49
Perna, R., Lazzati, D., & Giacomazzo, B. 2016, ApJL, 821, L18
Radcliffe, J. F., Beswick, R. J., Thomson, A. P., et al. 2019, MNRAS, 490, 4024
Ridnaia, A., Golenetskii, S., Aptekar, R., et al. 2020, GCN Circ., 26835, 1, https://gcn.gsfc.nasa.gov/gcn/gcn3/26835.gcn3
Rossi, A., Dadina, M., Maiorano, E., et al. 2019, GCN Circ., 26483, 1, https://gcn.gsfc.nasa.gov/gcn/gcn3/26483.gcn3
Rowlinson, A., & Anderson, G. E. 2019, MNRAS, 489, 3316
Sakamoto, T., Yoshida, A., Pal'Shin, V., et al. 2019, GCN Circ., 26481, 1, https://gcn.gsfc.nasa.gov/gcn/gcn3/26481.gcn3
Shenoy, V. & AstroSat CZTI Collaboration 2019, GCN Circ., 26511, 1, https://gcn.gsfc.nasa.gov/gcn/gcn3/26511.gcn3
Singer, L., Ahumada, T., Anand, S., et al. 2019, GCN Circ., 26479, 1, https://gcn.gsfc.nasa.gov/gcn/gcn3/26479.gcn3
Smith, G. P., Nicholl, M., Sharon, K., et al. 2019, GCN Circ., 26605, 1, https://gcn.gsfc.nasa.gov/gcn/gcn3/26605.gcn3
Smolčić, V., Novak, M., Bondi, M., et al. 2017, A&A, 602, A1
Stone, N. C., Metzger, B. D., & Haiman, Z. 2017, MNRAS, 464, 946
Sun, T., Zhang, C., Ping, Y., et al. 2019, GCN Circ., 26487, 1, https://gcn.gsfc.nasa.gov/gcn/gcn3/26487.gcn3
Tagawa, H., Haiman, Z., & Kocsis, B. 2020, ApJ, 898, 25
Verrecchia, F., Tavani, M., Cardillo, M., et al. 2019, GCN Circ., 26486, 1, https://gcn.gsfc.nasa.gov/gcn/gcn3/26486.gcn3
Wood, J. & Fermi-GBM Team, & GBM-LIGO/Virgo Group 2019, GCN Circ., 26461, 1, https://gcn.gsfc.nasa.gov/gcn/gcn3/26461.gcn3
Woosley, S. E. 2016, ApJL, 824, L10
Wright, E. L., Eisenhardt, P. R. M., Mainzer, A. K., et al. 2010, AJ, 140, 1868
Xu, D., Zhu, Z. P., Wang, H. J., et al. 2019, GCN Circ., 26478, 1, https://gcn.gsfc.nasa.gov/gcn/gcn3/26478.gcn3
Yamazaki, R., Asano, K., & Ohira, Y. 2016, PTEP, 2016, 051E01
Yanagisawa, K., Yoshida, M., Onozato, H., et al. 2019, GCN Circ., 26496, 1, https://gcn.gsfc.nasa.gov/gcn/gcn3/26496.gcn3
Yancey, C. C., Bear, B. E., Akukwe, B., et al. 2015, ApJ, 812, 168
Zhang, B. 2016, ApJL, 827, L31
Zhu, Z. P., Yu, B. Y., Xu, D., et al. 2019, GCN Circ., 26488, 1, https://gcn.gsfc.nasa.gov/gcn/gcn3/26488.gcn3